# Photoluminescence and Scintillation Mechanism of Cs4PbBr6

van Blaaderen, J.J.; van Hattem, A.; Mulder, J.T.; Biner, Daniel ; Krämer, Karl W.; Dorenbos, P.

**DOI**
10.1021/acs.jpcc.4c06347

**Publication date**
2024

**Document Version**
Final published version

**Published in**
The Journal of Physical Chemistry C

THE JOURNAL OF PHYSICAL CHEMISTRY C
A JOURNAL OF THE AMERICAN CHEMICAL SOCIETY



pubs.acs.org/JPCC
Article

# Photoluminescence and Scintillation Mechanism of $Cs_4PbBr_6$

J. Jasper van Blaaderen,* Andries van Hattem, Jence T. Mulder, Daniel Biner, Karl W. Krämer, and Pieter Dorenbos*

Cite This: J. Phys. Chem. C 2024, 128, 19921−19932
Read Online

ACCESS | Metrics & More | Article Recommendations | Supporting Information

**ABSTRACT:** Small bandgap scintillators have gained significant attention in recent years. Especially $Cs_4PbBr_6$ is an interesting material, mitigating the small Stokes shift-related problem of perovskites like $CsPbBr_3$. In this work, optical and scintillation properties of $Cs_4PbBr_6$ single crystals are investigated as a function of temperature, with a detailed focus at 10 K. The $Cs_4PbBr_6$ single crystals were grown using the vertical Bridgman method. Due to incongruent melting, $CsPbBr_3$ inclusions are formed, generating a 540 nm emission band. Prepairing $Cs_4PbBr_6$ via solid-state synthesis yields $CsPbBr_3$-inclusion-free material, showing no green 540 nm emission band. In $Cs_4PbBr_6$ samples with and without $CsPbBr_3$ inclusions, a new emission band at 610 nm ascribed to an unknown defect was found. Based on the presented experiments, an emission mechanism is proposed for $Cs_4PbBr_6$. This shows that both defects and $CsPbBr_3$ inclusions play a role in the emission behavior of $Cs_4PbBr_6$ but only the $CsPbBr_3$ inclusions are responsible for the 540 nm emission.

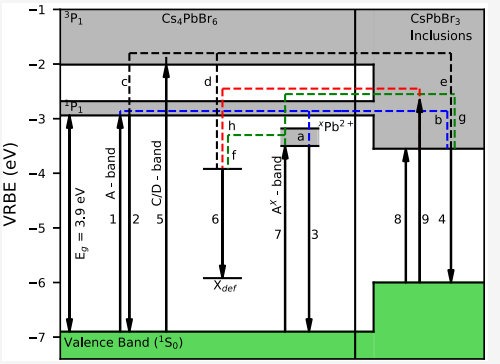




## I. INTRODUCTION

In the last 10 years, lead halide perovskites[1−3] and lead halide perovskite-related compounds[4−6] have gained interest in the field of X-ray and $\gamma$ photon scintillation detection. A clear distinction should be made, as discussed by Akkerman and Manna, between true perovskites and perovskite-related compounds.[7] The perovskite crystal structure, with stoichiometry $ABX_3$, consists of a three-dimensional network of corner-sharing $BX_6$ octahedra. The small bandgap of lead halide perovskites, approximately 3 eV, increases their theoretical maximum light yield compared to larger bandgap traditional scintillators.[1,8,9] Using eq 1 and a bandgap of 3 eV, it can be estimated that perovskites could surpass 100 000 photons/MeV scintillation photon yield.

$$N_{eh} = \frac{1\,000\,000}{\beta E_g}(e - h\ \text{pairs/MeV}) \quad (1)$$

Here, $N_{eh}$ represents the number of created electron−hole pairs, $\beta$ is taken to be ≈2.5, and $E_g$ represents the bandgap of the scintillator in eV. Perovskite-based scintillators differ from traditional scintillators, often doped or codoped, by being intrinsic scintillators, i.e., not relying on dopant ions.[10−14]

One of the shortcomings of lead halide perovskite-based scintillators, however, is their small Stokes shift, which results in losses due to self-absorption.[3,15,16] This problem has been addressed in detail by Wolszczak et al.[15] and Williams et al.[16] For other applications, like light-emitting diodes, this is a significantly smaller problem; these applications often use either thin films or nanocrystals.[17−19] Potential solutions to deal with the small Stokes shift of perovskites are lower-dimensional lead halide compounds or the introduction of a dopant to downshift the emission wavelength. Dimension, in this case, refers to the connectivity of the $PbX_6$ octahedral network. In the genuine perovskite structure, $ABX_3$, the $PbX_6$ network is conected in three dimensions. The dimensionality decreases to two-dimensional in compounds like $(PEA)_2PbBr_4$ or zero-dimensional in compounds like $Cs_4PbBr_6$. Lower-dimensional compounds often show self-trapped exciton emission which, compared to the near bandgap free exciton emission of perovskites, has a significantly larger Stokes shift.[20−23]

Examples of lower-dimensional lead-based compounds that have been studied for their scintillation properties are the two-dimensional hybrid organic−inorganic perovskites phenethylammonium lead bromide ($(PEA)_2PbBr_4$), butylammonium lead bromide ($(BA)_2PbBr_4$), and 2,2-(ethylenedioxy)bis-(ethylammonium) lead chloride ($(EDBE)PbCl_4$).[1,4,24,25] In these compounds, the cation located on the A site is replaced with a relatively large ammonium ion molecule, creating an alternating layered structure of $PbX_6$ octahedra and organic layers.

In this work, the low-temperature optical and scintillation properties of the zero-dimensional lead halide compound

Received: September 19, 2024
Revised: October 29, 2024
Accepted: November 4, 2024
Published: November 12, 2024

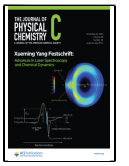

$Cs_4PbBr_6$ are studied. $Cs_4PbBr_6$ crystallizes in the $K_4CdCl_6$ structure with space group $R\bar{3}c$,[26,27] has a density of 4.19 g/cm$^3$, and a 3.9 eV bandgap.[28−30] Compared to the corner-sharing network of $BX_6$ octahedra in the perovskite crystal structure, the $A_4BX_6$ structure consists of isolated $BX_6$ octahedra.[31,32] This results in the formation of localized states, composed of the 6s$^2$ and 6s6p states of $Pb^{2+}$, on the $BX_6$ octahedra. This closely resembles low doping concentrations of $Pb^{2+}$ in face-centered cubic (fcc) alkali halide crystals, also resulting in the formation of isolated $[PbX_6]^{4-}$ octahedra.[29,33]

A general schematic of the energy levels of ions with an ns$^2$ electronic configuration, e.g., $Tl^+$, $Pb^{2+}$, and $Bi^{3+}$, is shown in Figure 1. The energy levels of a free ns$^2$ ion shift and split due

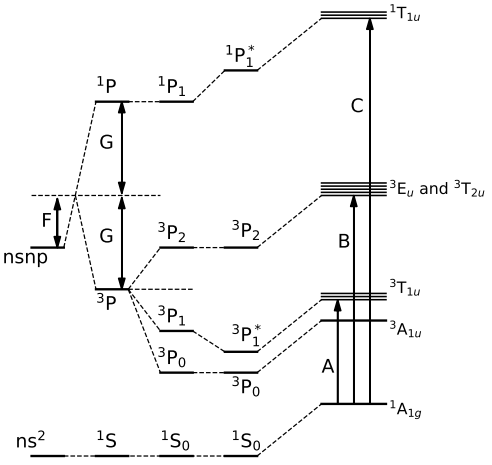


**Figure 1.** Schematic energy level diagram of ions with an ns$^2$ electronic ground state. Here, F represents the shift of the energy levels due to electrostatic interactions and G represents the shift due to exchange interactions. The final formation of the A-, B-, and C-bands and the corresponding symmetries are shown for an octahedrally surrounded ns$^2$ ion. The * indicates the mixing of the $^3P_1$ and $^1P_1$ levels due to spin−orbit interaction.

to a combination of electrostatic, exchange, and spin−orbit interactions.[34,35] In a crystal field, the levels will split further forming three distinct absorption bands, labeled the A ($^1S_0 \rightarrow {}^3P_1$), B ($^1S_0 \rightarrow {}^3P_2$), and C ($^1S_0 \rightarrow {}^1P_1$) band, which correspond with transitions between the ns$^2$ ground state and nsnp excited states.[34,35] The $^1S_0 \rightarrow {}^1P_1$ transition, or the C-band, is allowed. The $^1S_0 \rightarrow {}^3P_0$, $^1S_0 \rightarrow {}^3P_1$ (A-band), and $^1S_0 \rightarrow {}^3P_2$ (B-band) transitions are spin forbidden. The $^1S_0 \rightarrow {}^3P_1$ transition, or A-band, becomes partially allowed due to the spin−orbit coupling mixing the $^3P_1$ and $^1P_1$ states.[34] The $^1S_0 \rightarrow {}^3P_2$ transition, or B-band, can be induced due to vibrational coupling with the crystal lattice but it remains weak and often escapes observation.[35,36] Additionally, a fourth band, labeled the D-band, corresponding to a metal to metal charge transfer state between the ground state of $Pb^{2+}$ and the conduction band is often observed.[37,38] Emission typically takes place due to transitions from the $^3P_1$ (excited) state to the $^1S_0$ (ground) state and is commonly referred to as A-band emission.[34,35]

$Cs_4PbBr_6$ has been studied in different morphologies: nanocrystals,[28,39−42] thin films,[29,30,43] single crystals,[27,44,45] and powders.[46,47] Next to the potential interest of $Cs_4PbBr_6$ as a scintillator, it has also gained interest to be used in light-emitting diodes (LEDs),[48,49] luminescent solar concentrates,[50,51] and UV detectors.[52] Additionally, $Cs_4PbBr_6$ has been explored as host matrix for the production of $CsPbBr_3$ nanocrystals, an overview of which is presented by Akkerman et al.[52] $Cs_4PbBr_6$ especially gained a lot of interest due to its intense green 540 nm emission in addition to its UV 380 nm emission. The origin of the 540 nm emission is sometimes still under debate. It was suggested to either originate from bromine vacancies[27,41,53−55] or $CsPbBr_3$ nanocrystal inclusions.[29,30,45,56−60] The latter is seen as the more favorable explanation. This debate has recently been summarized in the review articles of Wang et al.,[61] Biswas,[62] and Akkerman et al.[52] In general, two different types of $Cs_4PbBr_6$ can be classified in the literature: $Cs_4PbBr_6$ with $CsPbBr_3$ inclusions, showing UV 380 nm and green 540 nm emission, and phase pure $Cs_4PbBr_6$, showing only UV 380 nm emission. The goal of this work is to propose a general emission mechanism for $Cs_4PbBr_6$, by studying the low-temperature optical and scintillation properties of $Cs_4PbBr_6$. The experiments are performed on a $Cs_4PbBr_6$ single crystal, grown using the vertical Bridgman method. One of the problems of producing single crystals from the melt, however, is the incongruent melting of $Cs_4PbBr_6$.[63] This results in the formation of $CsPbBr_3$ inclusions.[29,30] Such inclusions have also been observed in CsBr crystals doped with $Pb^{2+}$.[64−66] Zhang et al. demonstrated that $Cs_4PbBr_6$ single crystals can be grown from solution without $CsPbBr_3$ inclusions in the presence of an excess of $Cs^+$ and $Br^-$ ions, which stabilize the formation of $Cs_4PbBr_6$.[57] Akkermann et al. have demonstrated a similar approach for the production of $Cs_4PbBr_6$ nanocrystals.[28] We have chosen to use a solid-state synthesis, next to the Bridgman-grown single crystal, to produce a $Cs_4PbBr_6$ powder without $CsPbBr_3$ inclusions. The solid-state reaction between CsBr and $PbBr_2$ takes place below the incongruent melting point of $Cs_4PbBr_6$.[63] A slight excess of CsBr was chosen to prevent the formation of $CsPbBr_3$ inclusions. This approach has also been used for the synthesis of $Cs_4PbI_6$.[67]

In order to aid the presentation of the results and discussion presented in this work, Figure 2 shows the vacuum referred binding energy (VRBE) diagram applicable to $Cs_4PbBr_6$ on the left side and to $CsPbBr_3$ on the right side. The valence band of $Cs_4PbBr_6$ consists of bromine 4p orbitals and lead 6s orbitals while the conduction band consists of bromine 5p orbitals and lead 6s6p orbitals.[41,57,68] Vertical arrows represent excitation and emission transitions identified in the Section III. The horizontal dashed lines illustrate the energy and/or charge carrier transfer routes proposed in the Section IV.

## II. EXPERIMENTAL SECTION

Crystals of $Cs_4PbBr_6$ were grown by the vertical Bridgman technique in sealed silica ampules. Since $Cs_4PbBr_6$ melts incongruently at 500 °C,[63] a nonstoichiometric mixture of 75% CsBr and 25% $PbBr_2$ was used. CsBr (Fluka, >99.5%) and $PbBr_2$ ($\alpha$, 5N) were dried at 200 °C in vacuum. In a drybox, the starting materials were filled into a silica ampule and sealed off under vacuum. The mixture was molten at 550 °C and slowly cooled by moving the furnace within 10 days. The product contained a white tip of CsBr and $Cs_4PbBr_6$, a yellow-orange middle part of $Cs_4PbBr_6$, and an orange top part of $Cs_4PbBr_6$ and $CsPbBr_3$ eutecticum. $Cs_4PbBr_6$ crystals from the middle part were used for spectroscopic characterizations. Powder X-ray diffraction (Figure S1) and spectroscopic data revealed that the sample (middle part) contained about 90% $Cs_4PbBr_6$ and 10% $CsPbBr_3$. The phase separation in the CsBr-$PbBr_2$ melt did not work well, as can also be seen from the formation of a white tip containing CsBr.


https://doi.org/10.1021/acs.jpcc.4c06347
J. Phys. Chem. C 2024, 128, 19921−19932

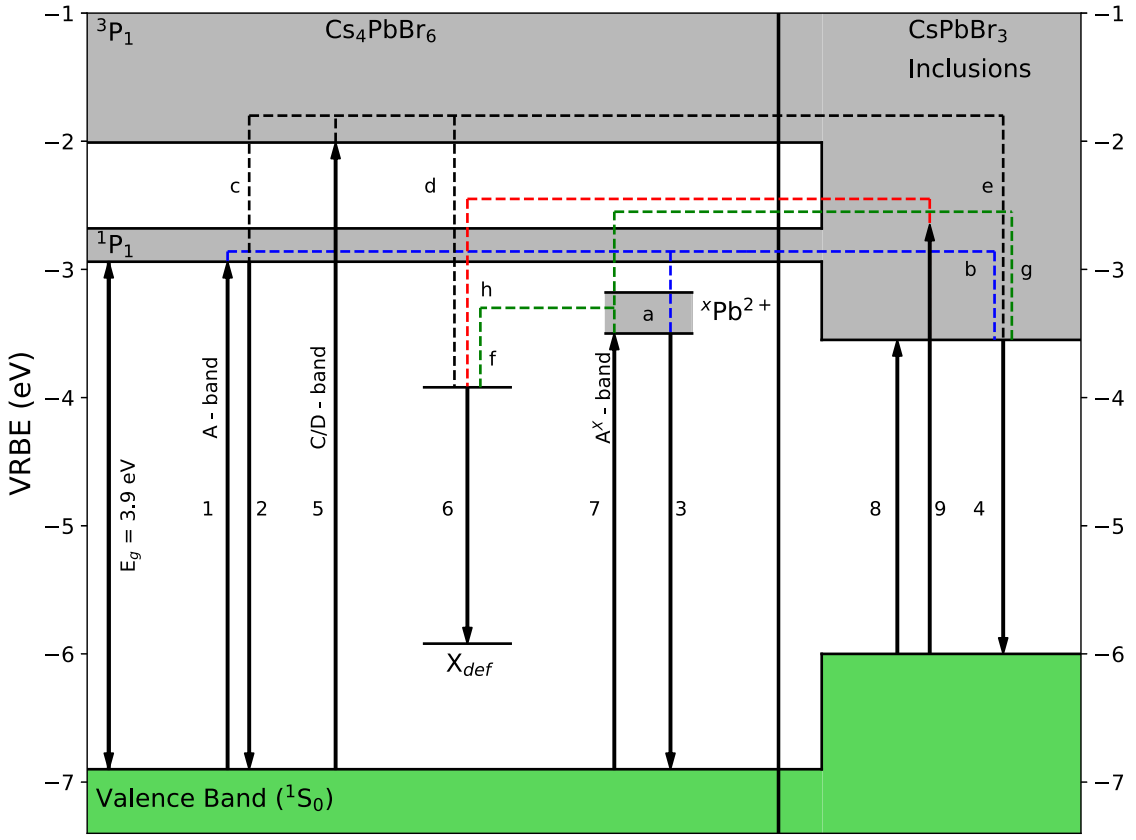


**Figure 2.** Vacuum referred binding energy (VRBE) diagram and the processes taking place in $Cs_4PbBr_6$ on the left and the VRBE plus additional processes taking place in $Cs_4PbBr_6$ with $CsPbBr_3$ inclusions on the right. Excitation and emission processes are represented by arrows and labeled using numbers. Energy transfer processes are indicated by dashed lines and labeled using letters. $X_{def}$ represents the defect-related emission, and $^xPb^{2+}$ represents $Pb^{2+}$ ions with a perturbed coordination shell.

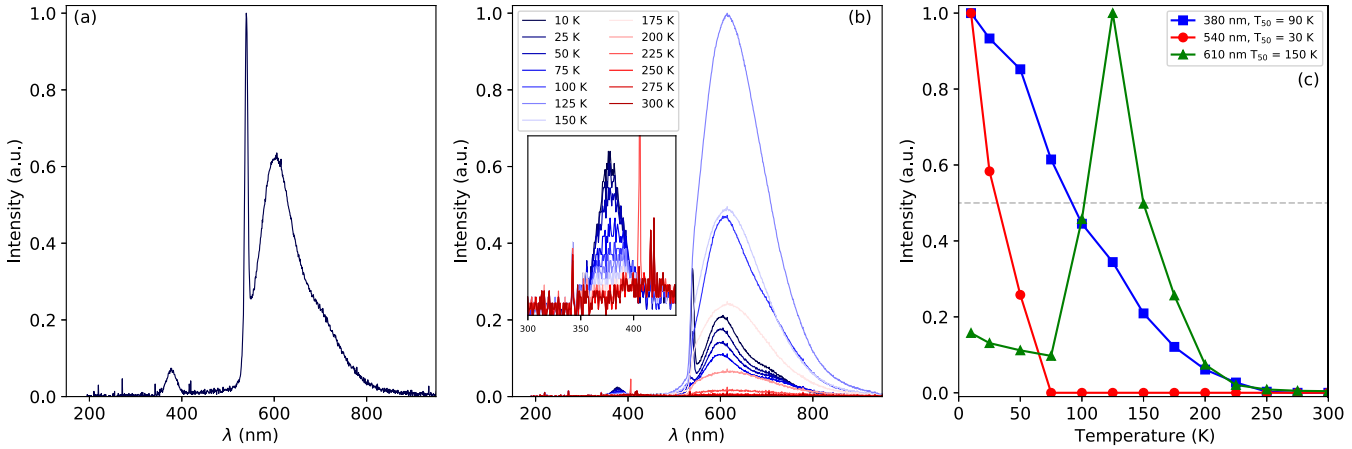


**Figure 3.** (a) X-ray excited emission spectrum of a $Cs_4PbBr_6$ single crystal with $CsPbBr_3$ inclusions recorded at 10 K. (b) Temperature-dependent X-ray excited emission spectra of a $Cs_4PbBr_6$ single crystal measured from 10 to 300 K. The inset shows a zoom in of the 380 nm emission peak. (c) Temperature-dependent integrated emission intensities of the 380, 540, and 630 nm emission bands.

CsBr (99.999%, Sigma-Aldrich) and $PbBr_2$ (>98%, Alfa Aesar) were mixed in a 4.024−1.000 ratio and ground for 15 min. The mixture was loaded in a closed crucible and heated for 48 h at 600 K, after which it was let to cool down to room temperature. The as-obtained powder was loaded in an X-ray diffraction sample holder closed with Kapton foil to prevent powder spreading and reaction with moisture. The sample was measured on a PANalytical X'Pert PRO using Cu K$\alpha$-radiation (45 kV, 40 mA) in the range $10° < 2\theta < 120°$ with an increment of 0.008° for a total measurement time of 9 h. The pattern was recorded using an X'Celerator detector. The obtained diffraction pattern was analyzed using Rietveld profile refinement[69,70] in the FullProf suite.[71,72] The analyzed powder diffraction pattern contained only the peaks of $Cs_4PbBr_6$ (>99%) and CsBr (<1%) as determined using Rietveld refinement.

X-ray excited emission spectra were recorded using a tungsten anode X-ray tube operated at 79 kV. This produces



https://doi.org/10.1021/acs.jpcc.4c06347
J. Phys. Chem. C 2024, 128, 19921−19932

X-rays with an average energy of 40 keV. The low-energy part of the produced X-ray spectrum was removed by placing a 3 mm aluminum filter in front of the X-ray tube. This prevented radiation damage. The samples were mounted on the coldfinger of a closed cycle helium cryostat operated below $10^{-4}$ bar.

Pulsed X-ray excited emission spectra were recorded by using the time-correlated single-photon counting method. The start signal of the measurements was generated by a PicoQuant LDH-P-C440 M pulsed laser, which directly excites a Hamamatsu N5084 light-excited X-ray tube. This results in the production of X-ray pulses with an average energy of 18.2 keV. The stop signal of the measurements was generated by the detection of a single photon by an ID Quantique id100-50 single-photon counter. Both start and stop signals were processed by an Ortec 567 time-to-amplitude converter whose output signal was digitized by an Ortex AD 144 16K ADC. The samples were mounted on the coldfinger of a closed cycle helium cryostat operated below $10^{-4}$ bar.

Photoluminescence excitation and emission spectra were recorded by using light from a 450 W xenon lamp passing through a Horiba Gemini 180 monochromator to excite the sample. The emitted light was collected at a 90° angle with respect to the excitation source. The emitted light passed through a Princeton Instruments SpectraPro-SP2358 monochromator before being detected by a Hamamatsu R7600u-20. Any reflected excitation light was removed by using a long-pass filter in front of the Princeton monochromator. All spectra were corrected for the lamp intensity. The samples were mounted on the coldfinger of a closed cycle helium cryostat operated below $10^{-4}$ bar.

The presented absorbance spectra were recorded using a PerkinElmer Lambda 1050 instrument equipped with an integrating sphere.

## III. RESULTS

**III.I. $Cs_4PbBr_6$ with $CsPbBr_3$ Inclusions.** Figure 3a shows the 10 K X-ray excited emission spectrum of the $Cs_4PbBr_6$ single crystal. The spectrum contains three emission bands at 380, 540, and 610 nm. These emission bands have also been observed by Kubota et al.[73] and Ding et al.[74] Wu et al. only studied the emission at wavelengths longer than 400 nm under X-ray excitation, hence only observing the 540 and 610 nm emissions.[75,76] The relative integral spectral intensities of the three emission bands are 1, 4.8, and 40.6, respectively. This means that the majority of the produced scintillation photons are present in the 610 nm emission band. The 380 nm UV band can be assigned to the intrinsic emission of $Cs_4PbBr_6$ (arrow 2 in Figure 2).[28,30,57,73] The powder X-ray diffraction pattern of the $Cs_4PbBr_6$ sample is shown in Figure S1 shows that the single crystal contains $CsPbBr_3$ related impurities to which the 540 nm emission can be ascribed (arrow 4 in Figure 2). It has been suggested by Kubota et al. that the 610 nm emission could be related to bromine vacancies (arrow 6 in Figure 2).[73−75]

The X-ray excited emission spectra, measured as a function of temperature, are shown in Figure 3b. The integrated intensities of the 380, 540, and 610 nm bands are shown in Figure 3c. The 540 nm emission band is fully quenched above 100 K. The intensity of the 610 nm emission shows a mild decrease until 75 K. Above 75 K, its intensity increases, reaching a maximum at 125 K, and then starts to quench. Based on the integrated peak intensities, the temperature ($T_{50}$) at which the intensity drops below 50% of its maximum intensity for the 380, 540, and 610 nm emissions is 90, 30, and 150 K, respectively.

The 10 K pulsed X-ray excited decay curve of the total emission spectrum of the $Cs_4PbBr_6$ single crystal is shown in Figure S2a. The inset shows the first 150 ns of the decay curve, where two decay components of 0.66 and 16.5 ns can be observed. On longer time scales, a significantly slower component of 770 ns can also be observed. The measurement was repeated by placing a 630 nm long-pass filter in front of the photodetector, removing the contribution of both the 380 and 540 nm emissions. The resulting decay curve is shown in Figure 4b, with the inset showing the first 150 ns of the decay. The decay curve no longer contains the sub-nanosecond decay component observed in Figure 4a. The decay contains three decay components of 10, 140, and 790 ns. Nikl et al. have studied the decay behavior of $Cs_4PbBr_6$ with $CsPbBr_3$ inclusions under photoexcitation finding a sub-nanosecond decay component for the 540 nm emission.[30] Additionally the sub-nanosecond decay component is similar to the decay curves measured on $CsPbBr_3$ single crystals under pulsed X-ray excitation.[3] This suggests that the sub-nanosecond decay component observed in Figure 3a can be assigned to the 540 nm emission.

Figure 5 shows the room-temperature absorbance spectrum of the $Cs_4PbBr_6$ single crystal, revealing two peaks at 260 nm (4.77 eV) and 315 nm (3.94 eV). An additional absorption edge is observed around 520 nm (2.38 eV). The 315 nm absorption band can be ascribed to the A-band transitions of $Pb^{2+}$ (arrow 1 in Figure 2). Kondo et al. ascribed the 260 nm band to a combination of the C- and D-band transitions.[29] The overlap of these two transitions has also been observed in alkali halides doped with low concentrations of $Pb^{2+}$ for example KBr which behaves similarly to $Cs_4PbBr_6$.[77,78] Hence, the 260 nm absorption band will be labeled as C/D-band transition (arrow 5 in Figure 2). The observed absorption edge, in Figure 5, around 520 nm (arrow 8 in Figure 2) can be ascribed to the presence of $CsPbBr_3$ inclusions.[29,30] For comparison, the absorption spectrum of a $CsPbBr_3$ single crystal is shown in Figure S2, revealing a similar absorption edge around 520 nm. Based on these similarities and the powder diffraction pattern of the $Cs_4PbBr_6$ single crystals, the 540 nm emission is ascribed to $CsPbBr_3$ inclusions (arrow 4 in Figure 2).

To further investigate the nature of the different absorption and emission bands, the photoluminescence emission of $Cs_4PbBr_6$ was measured as a function of the excitation wavelength at 10 K. The resulting image plot is shown in Figure 6a. From this image plot, two emission spectra are extracted at excitation wavelengths of 310 and 250 nm, as shown in Figure 6b,c, respectively. Upon excitation of the A-band (arrow 1 in Figure 2) at 310 nm, as shown in Figure 6b, two emission bands are observed at 378 and 540 nm. The 378 nm emission can be assigned to the intrinsic A-band emission of $Cs_4PbBr_6$ (arrow 2 in Figure 2),[30] and the 540 nm emission to the presence of $CsPbBr_3$ inclusions (arrow 4 in Figure 2).[19,29,30] Analogous behavior is observed in $Cs_4PbCl_6$ due to the presence $CsPbCl_3$ inclusions.[79] The excitation spectrum of the 378 nm A-band emission in Figure 6b shows two excitation bands at 250 and 310 nm. Similar to the absorbance spectrum shown in Figure 5, these are assigned to the C/D- and A-band transitions (arrows 1 and 5 in Figure 2), respectively. Note that the 310 nm excitation band actually consists of two bands, at 310 and 317 nm, which is typical of the A-band and caused by


https://doi.org/10.1021/acs.jpcc.4c06347
J. Phys. Chem. C 2024, 128, 19921−19932

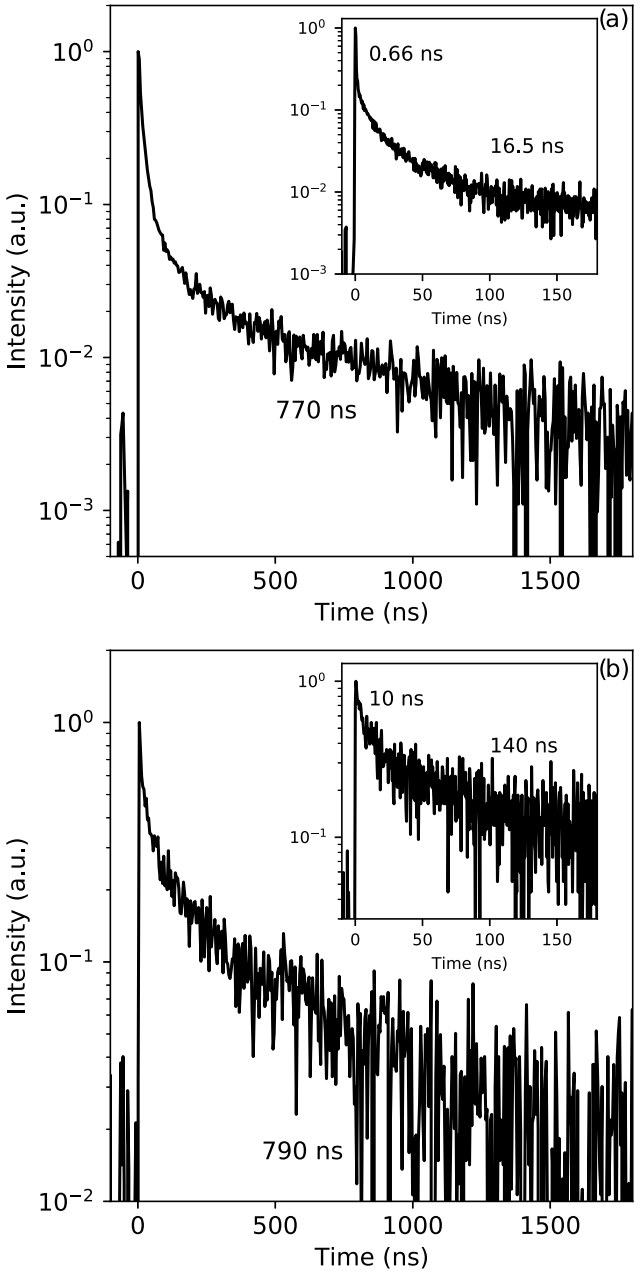


**Figure 4.** (a) Pulsed X-ray excited decay curve of the total emission spectrum of a $Cs_4PbBr_6$ single crystal with $CsPbBr_3$ inclusions at 10 K. (b) Pulsed X-ray excited decay curve, recorded by placing a 630 nm long-pass filter in front of the detector, of a $Cs_4PbBr_6$ single crystal with $CsPbBr_3$ inclusions at 10 K.

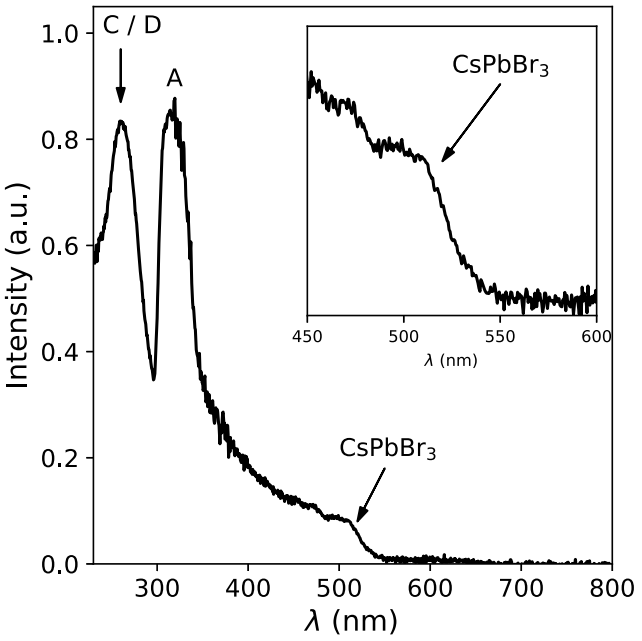


**Figure 5.** Room-temperature absorbance spectrum of a $Cs_4PbBr_6$ single crystal with $CsPbBr_3$ inclusions; the inset shows a zoom-in of the feature observed between 500 and 550 nm.

a Jahn−Teller splitting.[34,35] From the image plot in Figure 6a, it can be observed that the 378 nm emission band excited via the A band transition is the most intense emission band observed.

Upon excitation in the C/D-band (arrow 5 in Figure 2) at 250 nm, as shown in Figure 6c, two main emission bands at 378 and 610 nm are observed (arrows 2 and 6 in Figure 2). The 540 nm band is also present in the form of a shoulder on the shorter-wavelength side of the 610 nm band. The 610 nm emission band has not been observed before under photoexcitation but is the dominant emission band under X-ray excitation, as shown in Figure 3a. The excitation spectrum, recorded at 675 nm, in Figure 6c shows an intense 250 nm C/D- and a weak 310 nm A-band, which are also observed in Figure 6b but with a much different intensity ratio. Additionally, a second Jahn−Teller split A-band, (arrow 7 in Figure 2) is observed at 325 and 332 nm which is labeled as $A^X$ and there is also an excitation band at 370 nm, attributed to the $CsPbBr_3$ inclusions.[34,35] Upon excitation at 370 nm (arrow 9 in Figure 2), two emission bands are observed at 540 and 610 nm, as shown in Figure 6d. The excitation spectrum recorded at 545 nm is also shown in Figure 6d.

The quenching behavior under optical excitation is similar to the quenching behavior under X-ray excitation. The $T_{50}$ values for the 378, 540, and 600 nm emissions are approximately 110, 60, and 160 K. The temperature dependence of the different emission bands upon exciting at the 250 nm C/D-band, 310 nm A-band, and 370 nm $CsPbBr_3$ inclusions is shown in Figure S3.

**III.II. $Cs_4PbBr_6$ without $CsPbBr_3$ Inclusions.** $Cs_4PbBr_6$ without $CsPbBr_3$ inclusions was synthesized using a solid-state synthesis. After the heat treatment of the CsBr:$PbBr_2$ (4:1) mixture, a light gray powder was obtained. The X-ray diffraction pattern of the synthesized material only exhibits diffraction peaks of $Cs_4PbBr_6$ and CsBr. The diffraction pattern is shown in Figures S4 and S5 together with a two-phase Rietveld profile refinement. The refinement yielded expected mass fractions of >99% for $Cs_4PbBr_6$ and <1% for CsBr. In contrast to the diffraction pattern of the $Cs_4PbBr_6$ single crystal, no peaks related to $CsPbBr_3$ were observed.

To investigate the nature of the different absorption and emission bands of $Cs_4PbBr_6$ without $CsPbBr_3$ inclusions, the photoluminescence emission was measured as a function of the excitation wavelength at 10 K. The resulting image plot, plotted on a log scale, is shown in Figure 7a. From the image plot, two emission spectra are extracted at excitation wavelengths of the 310 nm A-band and 250 nm C/D-band, shown in Figure 7b,c, respectively. Upon excitation of the A-band (arrow 1 in Figure 2), two emission bands at 378 and 455 (arrows 2 and 3 in Figure 2) are observed. The 540 nm


https://doi.org/10.1021/acs.jpcc.4c06347
J. Phys. Chem. C 2024, 128, 19921−19932

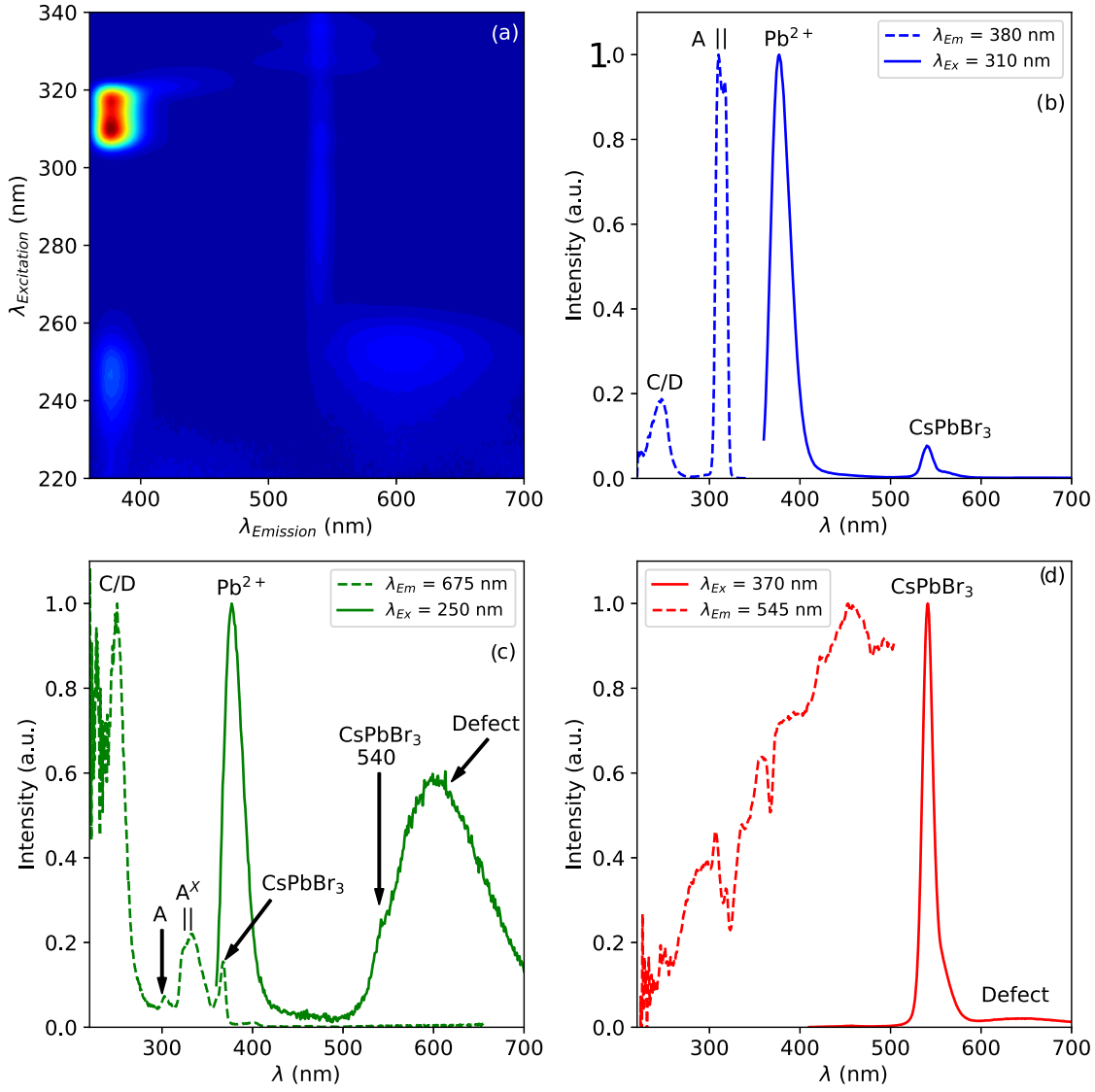


**Figure 6.** (a) Photoluminescence emission intensity of a $Cs_4PbBr_6$ single crystal with $CsPbBr_3$ inclusions as a function of excitation wavelength at 10 K. Photoluminescence excitation and emission spectra at 10 K measured at emission and excitation wavelengths of (b) 380 and 310 nm, (c) 675 and 250 nm, and (d) 545 and 370 nm, respectively.

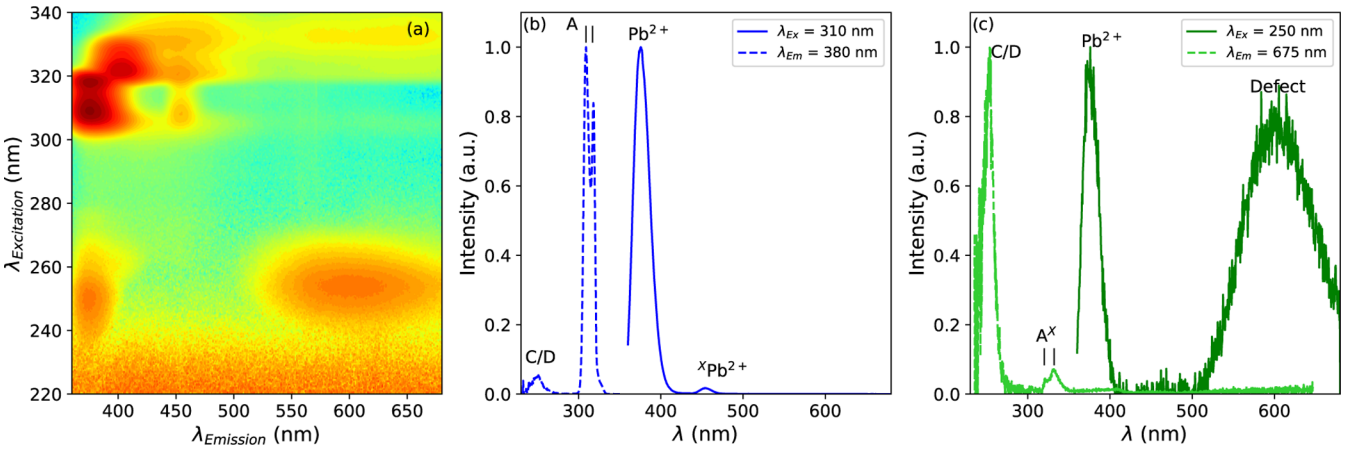


**Figure 7.** (a) Photoluminescence emission intensity of $Cs_4PbBr_6$ without $CsPbBr_3$ inclusions as a function of excitation wavelength at 10 K, on a log scale. Photoluminescence excitation and emission spectra at 10 K measured at emission and excitation wavelengths of (b) 380 and 310 nm and (c) 675 and 250 nm, respectively.



https://doi.org/10.1021/acs.jpcc.4c06347
J. Phys. Chem. C 2024, 128, 19921−19932

emission (arrow 4 in Figure 2), observed in Figure 6b and related to the $CsPbBr_3$ inclusions, is no longer present. The excitation spectrum of the 378 nm A-band $Pb^{2+}$ emission, in Figure 7b, shows the C/D-band at 250 nm and the strong Jahn−Teller split A-band at 310 and 317 nm.[34,35] Upon excitation of the C/D band (arrow 5 in Figure 2) both the 378 nm A-band emission and 610 nm emission (arrows 2 and 6 in Figure 2) are observed. The excitation spectrum recorded at 675 nm, in Figure 7c, contains the C/D band at 250 nm and the Jahn−Teller split $A^X$-band at 320 and 332 nm.

Figure 8 shows the 10 K X-ray excited emission spectrum of $Cs_4PbBr_6$ without $CsPbBr_3$ inclusions. Two emission bands are observed at 380 and 610 nm with relative intensities of 1 and 25, respectively. The $T_{50}$ temperature for both emission bands is 150 K as was obtained from temperature-dependent behavior of both bands, as shown in Figure S6a,b.

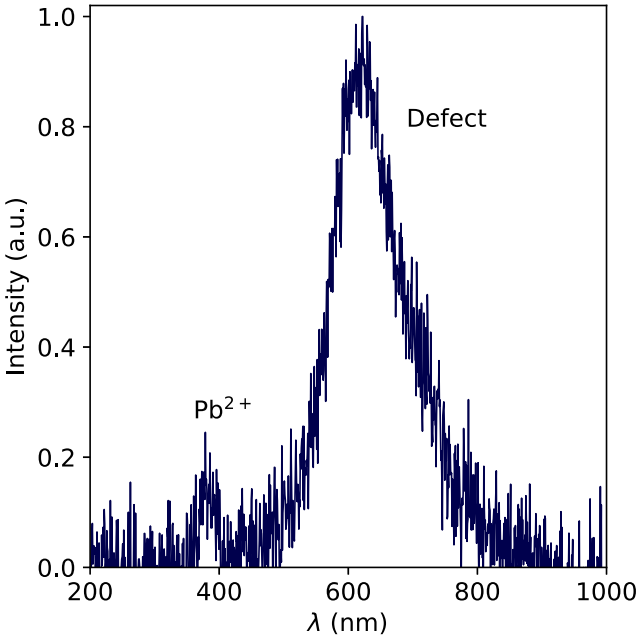


**Figure 8.** X-ray excited emission spectrum of $Cs_4PbBr_6$ without $CsPbBr_3$ inclusions recorded at 10 K.

## IV. DISCUSSION

**IV.I. Perturbed $Pb^{2+}$ Coordination Sphere.** Depending on the emission wavelength at which the excitation spectra are recorded, two different A-excitation bands are observed. A comparison of the two excitation bands for $Cs_4PbBr_6$ with and without $CsPbBr_3$ inclusions is shown in Figure 9a,b, respectively. Figure 9c shows three emission spectra excited at 310 nm (only A-band transition, arrow 2 in Figure 2), 320 nm (mixed A- and $A^X$-band transitions), and 332 nm (only $A^X$-band transition, arrow 7 in Figure 2) of the $Cs_4PbBr_6$ sample without $CsPbBr_3$ inclusions. Exciting only in the A-band yields two emission bands at 378 nm (strong) and 455 nm (weak). Exciting in the $A^X$-band yields three emission bands at 405, 455, and 610 nm. It is known that the presence of defects close to $Pb^{2+}$ ions influences both the excitation and emission properties of $Pb^{2+}$ ions.[80] This has been studied extensively in the alkali halides.[81−88] Based on these observations, the A-band excitation and A-band emission (arrows 1 and 2 in Figure 2, respectively) are attributed to originate from a $Pb^{2+}$ ion on an unperturbed site. The $A^X$-band (arrow 7 in Figure 2) and the 405 and 455 nm emission bands (arrow 3 in Figure 2) originate from a $Pb^{2+}$ ion with a different or perturbed coordination shell. The presence of two additional emission bands points to at least two different perturbed coordination spheres of $Pb^{2+}$. These could, for example, be a $Pb^{2+}$ interstitial, a bromine vacancy next to $Pb^{2+}$, or $Pb^{2+}$ on a $Cs^+$ site.

After exciting the A-band transition, next to A-band emission, energy transfer to a $Pb^{2+}$ ion with a perturbed coordination sphere can take place, as evident from the 455 nm emission band in Figure 7b. Energy transfer can also take place to the $CsPbBr_3$ inclusions, if present, as evident from the 540 nm emission band in Figure 6b. After exciting the $A^X$-band, next to the 405 and 455 nm emissions, the 610 nm emission band can also be observed, as seen in Figure 9c.

**IV.II. Defect-Related Emission.** The 610 nm emission band is mainly observed upon exiting the C/D-band at 250 nm, as evident from the intensities of the excitation bands shown in Figures 6c and 7c. It is also possible to observe the

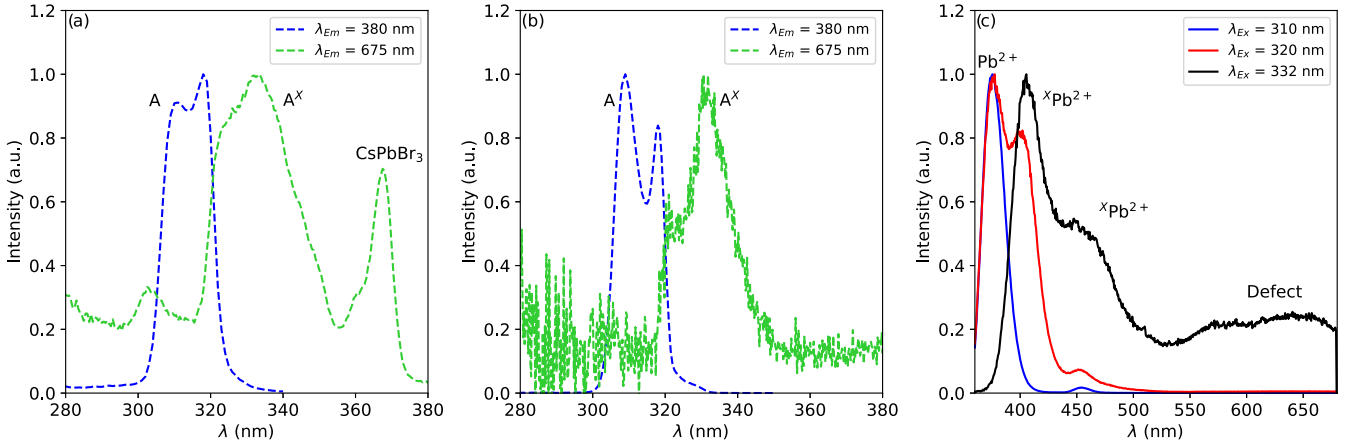


**Figure 9.** Comparison of the A-band transitions of (a) $Cs_4PbBr_6$ with $CsPbBr_3$ inclusions and (b) $Cs_4PbBr_6$ without $CsPbBr_3$ inclusions. The two excitation spectra shown for both forms of $Cs_4PbBr_6$ are recorded at 380 and 675 nm. The A-band transition of $Pb^{2+}$ ions with an unperturbed coordination sphere is labeled A and that of $Pb^{2+}$ ions with a perturbed coordination sphere is labeled $A^X$. (c) Emission spectra of $Cs_4PbBr_6$ without $CsPbBr_3$ inclusions excited in the A- and $A^X$-bands.



https://doi.org/10.1021/acs.jpcc.4c06347
J. Phys. Chem. C 2024, 128, 19921−19932

610 nm emission upon exciting the $A^X$-band, excluding D-band emission[89−91] as potential explanation. The 610 nm emission excitation via the A-band is weak, excitation via the $A^X$-band is significantly stronger as shown in Figure 6c. This all suggests that the 610 nm emission originates from a defect in the vicinity of a $Pb^{2+}$ ion, resulting in a perturbation of the coordination sphere of $Pb^{2+}$ and the observation of the $A^X$-band. The 610 nm emission band cannot be excited directly. The defect seems to first need to trap a mobile charge carrier before it can become emissive. This can happen by exciting the C/D-band, upon which mobile charge carriers are created, or via excitation of a $CsPbBr_3$ inclusion well above the bandgap, at 370 nm (arrow 9 in Figure 2), or a $Pb^{2+}$ ion with a perturbed coordination sphere, illustrated by energy transfer pathways d, h, and f in Figure 2, respectively. The excitation spectra of the 610 nm emission, Figures 6c and 7c, show that exciting the C/D band is the dominant pathway to excite the defects.

**IV.III. Inclusion-Related Emission.** The emission peak, linked to the $CsPbBr_3$ inclusions, was located at 540 nm in the $Cs_4PbBr_6$ single crystals used in this work. The green $CsPbBr_3$ inclusion emission in nanocrystals however is typically reported to be located from 515 to 524 nm.[52] It has been demonstrated by Chen et al. and Almeida et al., in $Cs_4PbBr_6$ nanocrystals with $CsPbBr_3$ inclusions, that the emission wavelength of the $CsPbBr_3$ emission can be tuned by altering the synthesis and effectively changing the size of the $CsPbBr_3$ inclusions.[45,92] The 540 nm emission wavelength observed in this work matches with the emission wavelength observed for bulk $CsPbBr_3$.[3] This suggests that during the synthesis process from the melt $CsPbBr_3$ domains are formed large enough to not be influenced by confinement effects and show bulk properties. When $Cs_4PbBr_6$ with $CsPbBr_3$ inclusions is excited at wavelengths longer than 350 nm it is possible to directly excite the $CsPbBr_3$ inclusions, as demonstrated in Figure 6d. The inclusions can also be excited by an energy transfer process from either the A-band, C/D-band, or a $Pb^{2+}$ ion with a perturbed coordination sphere, illustrated by energy transfer pathways b, e, and g in Figure 2, respectively.

**IV.IV. Excitation and Emission Mechanism.** Based on the results and discussion, a vacuum referred binding energy diagram can be constructed to explain the observed emission processes. The resulting diagram is shown in Figure 2. Based on computational methods presented by Kang et al.[68] and information from He et al.[93] we tentatively placed the valence band (VB) top of $Cs_4PbBr_6$ at −7 eV and that of $CsPbBr_3$ 1 eV higher. The optical bandgap of $Cs_4PbBr_6$, which equals the A-band transition energy, is 3.9 eV. This value has been determined experimentally.[29,94] The bottom of the conduction band (CB) of $Cs_4PbBr_6$ is determined by adding the optical bandgap to the VRBE of the top of the VB. The CB-bottom of $CsPbBr_3$ is determined by adding the emission energy to the VRBE of its VB-top; due to the small Stokes shift of $CsPbBr_3$, it can be assumed that the emission energy is approximately equal to the optical bandgap. It is estimated that the error margins in placing the top of the VB are approximately ±0.3 eV; essential is that the VB-top and CB-bottom of $CsPbBr_3$ fall both well inside the bandgap of $Cs_4PbBr_6$. The C/D-band transition energy is defined as the mobility bandgap, where mobile charge carriers are created upon excitation. The position of the A- and C/D-band transitions is determined based on the excitation spectra shown in Figures 6b and 7b.

The diagram consists of two sections: on the left, the processes taking place in $Cs_4PbBr_6$. On the right, the additional processes are taking place due to the presence of $CsPbBr_3$ inclusions. The position of the $A^X$-band transitions, labeled $^X Pb^{2+}$ are determined using Figures 6c and 7c. The exact position of the defect-related energy levels, labeled $X_{def}$ in the diagram, is uncertain. The spacing between the levels is based of the emission wavelength of the defect-related emission.

After exciting the A-band (arrow 1), three processes can take place: A-band emission (arrow 2), or energy transfer (pathways a and b) resulting in emission from a $^X Pb^{2+}$ ion (arrow 3) or $CsPbBr_3$ inclusion (arrow 4). After exciting the C/D-band (arrow 5), three different processes can take place: A-band emission (arrow 2), or energy and/or charge carrier transfer (pathways d and e), resulting in emission from a defect (arrow 6) or $CsPbBr_3$ inclusions (arrow 4). It is also possible to excite a $^X Pb^{2+}$ ion (arrow 7) after which three processes can take place: $A^X$-band emission (arrow 3) or energy transfer (pathways f and g) resulting in emission from a defect (arrow 6) or $CsPbBr_3$ inclusions (arrow 4). The $CsPbBr_3$ inclusions can also be excited directly (arrows 8 and 9) after which two processes can take place: emission from the inclusion (arrow 4) or energy transfer (pathway h) if excited well above the bandgap (arrow 9), resulting in emission from a defect (arrow 6).

**IV.V. X-ray Versus Optical Excitation.** Under X-ray excitation, as shown in Figure 3a, the 610 nm emission band is 40.6 times more intense compared with the A-band emission. Upon exciting the C/D-band the intensity of the 610 nm emission is only 2.5 times stronger compared to the A-band emission. Moreover, it is completely absent upon exciting the A-band. The observed intensity difference can be explained based on the difference between X-ray excitation and optical excitation. Upon X-ray excitation, all energy of the incident X-ray is transferred to a primary electron. This hot electron creates secondary excitations via electron−electron interactions along its ionization track. This results in the formation of spatially separated electrons and holes. The electrons, due to their larger mobility, will diffuse further away from the initial ionization track compared to the holes.[95−98] The separated electrons and holes first need to approach each other before emission can take place. Upon optically exciting the C/D-band transition, the formed electrons and holes stay in closer proximity; emission can take place immediately. This happens on a shorter time scale compared to the recombination of the spatially separated electrons and holes formed upon X-ray excitation. The latter thus have more time to move through the crystal lattice and find a defect, thus leading to a more intense 610 nm emission band upon X-ray excitation.

## V. CONCLUSIONS

In this work, the zero-dimensional cesium lead halide compound $Cs_4PbBr_6$ has been studied as a function of temperature under both X-ray and UV−vis excitation. $Cs_4PbBr_6$ is studied with and without $CsPbBr_3$ inclusions. Upon X-ray excitation, most of the scintillation light is present in the 610 nm emission band for both forms of $Cs_4PbBr_6$. This is ascribed to the formation of spatially separated charge carriers reaching lattice defects. The pulsed X-ray excited decay curves show multiple decay components, the longest being approximately 800 ns. Upon exciting the C/D-band at 250 nm, the 610 nm emission band was also found which has not been reported before. The excitation spectrum of the 610 nm emission band contains an excitation band, labeled $A^X$, which is ascribed to $Pb^{2+}$ ions with a perturbed coordination sphere. It


https://doi.org/10.1021/acs.jpcc.4c06347
J. Phys. Chem. C 2024, 128, 19921−19932

is suggested that the 610 nm emission originates from defects in the vicinity of $Pb^{2+}$ ions, leading to the contraction of the coordination sphere. The 540 nm emission, based on the X-ray diffraction patterns and absorption spectra, is assigned to the presence of $CsPbBr_3$ inclusions. It is thus shown experimentally that both $CsPbBr_3$ inclusions and defects play a role in the photoluminescence behavior of $Cs_4PbBr_6$. All experimental results could be combined to formulate a general mechanism for the emission behavior of $Cs_4PbBr_6$.

## ■ ASSOCIATED CONTENT

### Supporting Information

The Supporting Information is available free of charge at https://pubs.acs.org/doi/10.1021/acs.jpcc.4c06347.

Photoluminescence and scintillation mechanism of Cs $_4$PbBr$_6$ (ZIP)

X-ray diffraction pattern of $Cs_4PbBr_6$ grown using the vertical Bridgman method; absorbance spectrum of a $CsPbBr_3$ single crystal; temperature-dependent photoluminescence emission spectra and integrated intensities of $Cs_4PbBr_6$ single crystal upon exciting at 250, 310, and 370 nm; X-ray diffraction pattern of synthesized $Cs_4PbBr_6$ powder; and temperature-dependent X-ray excited emission spectra of synthesized $Cs_4PbBr_6$ powder (PDF)

## ■ AUTHOR INFORMATION


### Corresponding Authors

**J. Jasper van Blaaderen** − *Faculty of Applied Sciences, Department of Radiation Science and Technology, Delft University of Technology,, 2629 JB Delft, The Netherlands;* orcid.org/0000-0003-1460-8319; Email: J.J.vanBlaaderen@tudelft.nl

**Pieter Dorenbos** − *Faculty of Applied Sciences, Department of Radiation Science and Technology, Delft University of Technology,, 2629 JB Delft, The Netherlands;* Email: P.Dorenbos@tudelft.nl

### Authors

**Andries van Hattem** − *Faculty of Applied Sciences, Department of Radiation Science and Technology, Delft University of Technology,, 2629 JB Delft, The Netherlands;* orcid.org/0000-0001-8814-4049

**Jence T. Mulder** − *Faculty of Applied Sciences, Optoelectronic Materials Section, Delft University of Technology,, 2629 HZ Delft, The Netherlands;* orcid.org/0000-0002-4397-1347

**Daniel Biner** − *Department of Chemistry, Biochemistry, and Pharmaceutical Sciences, Univeristy of Bern, 3012 Bern, Switzerland*

**Karl W. Krämer** − *Department of Chemistry, Biochemistry, and Pharmaceutical Sciences, Univeristy of Bern, 3012 Bern, Switzerland*

Complete contact information is available at: https://pubs.acs.org/10.1021/acs.jpcc.4c06347


### Author Contributions

The manuscript was written through contributions of all authors. All authors have given approval to the final version of the manuscript.

### Notes

The authors declare no competing financial interest.

## ■ ACKNOWLEDGMENTS

The authors thank John Vlieland for his help in the solid-state synthesis process. The authors acknowledge financial support from the TTW/OTP grant no. 18040 of the Dutch Research Council.

## ■ REFERENCES


(1) Bitowosuto, M. D.; Cortecchia, D.; Drozdowski, W.; Brylew, K.; Lachmanski, W.; Bruno, A.; Soci, C. X-ray Scintillation in Lead Halide Perovskite Crystals. *Sci. Rep.* **2016**, *6*, No. 37254.

(2) Li, Y.; Shao, W.; Ouyang, X.; Zhu, Z.; Zhang, H.; Ouyang, X.; Liu, B.; Xu, Q. Scintillation Properties of Perovskite Single Crystals. *J. Phys. Chem. C* **2019**, *123* (28), 17449−17453.

(3) van Blaaderen, J. J.; Biner, D.; Kramer, K. W.; Dorenbos, P. The Temperature Dependent Optical and Scintillation Characterisation of Bridgman Grown $CsPbX_3$ (X = Br, Cl) Single Crystals, Nuclear Instruments. *Nucl. Instrum. Methods Phys. Res., Sect. A* **2024**, *1064*, No. 169322.

(4) van Blaaderen, J. J.; Maddalena, F.; Dong, C.; Birowosuto, M. D.; Dorenbos, P. Temperature Dependent Scintillation Properties and Mechanisms of $(PEA)_2PbBr_4$ Single Crystals. *J. Mater. Chem. C* **2022**, *10*, 11598−11606.

(5) van Blaaderen, J. J.; van der Sar, S.; Onggo, D.; K Sheikh, M. A.; Schaart, D. R.; Birowosuto, M. D.; Dorenbos, P. $(BZA)_2PbBr_4$: A Potential Scintillator for Photon-Counting Computed Tomography Detectors. *J. Lumin.* **2023**, *263*, No. 120012.

(6) van Blaaderen, J. J.; van den Brekel, L. A.; Kramer, K. W.; Dorenbos, P. Scintillation and Optical Characterisation of $CsCu_2I_3$ Single Crystals from 10 to 400K. *Chem. Mater.* **2023**, *35*, 9623−9631.

(7) Akkerman, Q. A.; Manna, L. What Defines a Halide Perovskite? *ACS Energy Lett.* **2020**, *5*, 604−610.

(8) Dorenbos, P. The Quest for High Resolution $\gamma$-Ray Scintillators. *Opt. Mater.: X* **2019**, *1*, No. 100021.

(9) Dorenbos, P. Fundamental Limitations in the Performance of $Ce^{3+}$-, $Pr^{3+}$-, and $Eu^{2+}$- Activated Scintillators. *IEEE Trans. Nucl. Sci.* **2010**, *57* (3), 1162−1167.

(10) van Loef, E. V. D.; Dorenbos, P.; van Eijk, C. W. E.; et al. High-Energy-Resolution Scintillator: $Ce^{3+}$ activated $LaBr_3$. *Appl. Phys. Lett.* **2001**, *79*, 1573.

(11) Alekhin, M. S.; Biner, D. A.; Krämer, K. W.; Dorenbos, P. Optical and Scintillation Properties of $CsBa_2I_5$:$Eu^{2+}$. *J. Lumin.* **2014**, *145*, 723−728.

(12) Bourret-Courchesne, E. D.; Bizarri, G.; Borade, R.; Yan, Z.; Hanrahan, S. M.; Gundiah, G.; Choudhry, A.; Canning, A.; Derenzo, S. E. $Eu^{2+}$-Doped $CsBa_2I_5$, a New High-Performance Scintillator. *Nucl. Instrum. Methods Phys. Res. A* **2009**, *612*, 138−142.

(13) van Aarle, C.; Krämer, K. W.; Dorenbos, P. Avoiding Concentration Quenching and Self-Absorption in $Cs_4EuX_6$ (X = Br, I) by $Sm^{2+}$ Doping. *J. Mater. Chem. C* **2023**, *11*, 2336−2344.

(14) van Aarle, C.; Krämer, K. W.; Dorenbos, P. Characterisation of $Sm^{2+}$-Doped $CsYbBr_3$, $CsYbI_3$ and $YbCl_2$ for Near-Infrared Scintillator Application. *J. Lumin.* **2022**, *251*, No. 119209.

(15) Wolszczak, W. W.; Carrroll, D. L.; Williams, R. T. *Advanced X-ray Detector Technologies*, Chapter 1Springer, 2022.

(16) Williams, R. T.; Wolszczak, W. W.; Yan, X.; Carrol, D. L. Perovskite Quantum-Dot-in-Host for Detection of Ionising Radiation. *ACS Nano* **2020**, *14*, 5161−5169.

(17) Saki, Z.; Byranvand, M. M.; Taghavinia, N.; Kedia, M.; Saliba, M. Solution-Processed Perovskite Thin-Films: The Journey from Lab- to Large-Scale Solar Cells. *Energy Environ. Sci.* **2021**, *14*, 5690−5722.

(18) Dunlap-Shohl, W. A.; Zhou, Y.; Padture, N. P.; Mitzi, D. B. Synthetic Approaches for Halide Perovskite Thin Films. *Chem. Rev.* **2019**, *119*, 3193−3295.

(19) Akkerman, Q. A.; Raino, G.; Kovalenko, M. V.; Manna, L. Genesis, Challenges and Opportunities for Colloidal Lead Halide Perovskite Nanocrystals. *Nat. Mater.* **2018**, *17*, 394−405.

(20) Song, K. S.; Williams, R. T. *Springers Series in Solid State Sciences, Self traped Excitons*, 2nd ed.; SpringerVerlag: Berlin, 1996; p 105.
(21) Yuan, Z.; Zhou, C.; Tian, Y.; Shu, Y.; Messier, J.; Wang, J. C.; van de Burght, L. J.; Kountouriotis, Y.; Xin, E.; Holt, E.; et al. One-Dimensional Organic Lead Halide Perovskite with Efficient Bluish White-Light Emission. *Nat. Commun.* **2017**, *8*, No. 14051.
(22) Dohner, E. R.; Jaffe, A.; Bradshaw, L. R.; Karunadasa, H. I. Intrinsic White-Light Emission from Layered Hybrid Perovskites. *J. Am. Chem. Soc.* **2014**, *136* (38), 13154−13157.
(23) Mao, L.; Wy, Y.; Stoumpos, C. C.; Wasielewski, M. R.; Kanatzidis, M. G. White-Light Emission and Structural Distortion in New Corrugated Two-Dimensinal Lead Bromide Perovskties. *J. Am. Chem. Soc.* **2017**, *139* (14), 5210−5215.
(24) Maddalena, F.; Xie, A.; Arramel; Witkowski, M. E.; Makowski, M.; Mahler, B.; Drozdowski, W.; Mariyappan, T.; Springham, S. V.; Coquet, P.; et al. Effect of Commensurate Lithium Doping on the Scintillation of Two-Dimensional Perovskite Crystals. *J. Mater. Chem. C* **2021**, *9*, 2504.
(25) Xie, A.; Maddalena, F.; Witkowski, M. E.; Makowski, M.; Mahler, B.; Drozdowski, W.; Springham, S. V.; Coquet, P.; Dujardin, C.; Birowosuto, M. D.; Dang, C. Library of Two-Dimensional Hybrid Lead Halide Perovskite Scintillator Crystals. *Chem. Mater.* **2020**, *32*, 8530−8539.
(26) MØller, C. K.*On the Structure of Cesium Hexahalogeno-Plumbates (II)*; Copenhagen: Denmark: Munksgaard, 1960; Vol. *32*, pp 1−13.
(27) De Bastiani, M.; Dursun, I.; Zhang, Y.; Alshankiti, B. A.; Miao, X.-H.; Yin, J.; Yengel, E.; Alarousu, E.; Turedi, B.; Almutlaq, J. M.; et al. Inside Perovskites: Quantum Luminescence from Bulk $Cs_4PbBr_6$ Single Crystals. *Chem. Mater.* **2017**, *29*, 7108−7113.
(28) Akkerman, Q. A.; Park, S.; Radicchi, E.; Nunzi, F.; Mosconi, E.; De Angelis, F.; Brescia, R.; Rastogi, P.; Prato, M.; Manna, L. Nearly Monodisperse Insulator $Cs_4PbX_6$ (X = Cl, Br, I) Nanocrystals, Their Mixed Halide Compositions, and Their Transformation into $CsPbX_3$ Nanocrystals. *Nano Lett.* **2017**, *17*, 1924−1930.
(29) Kondo, S.; Amaya, K.; Saito, T. Localised Optical Absorption in $Cs_4PbBr_6$. *J. Phys.: Condens. Matter* **2002**, *14*, 2093−2099.
(30) Nikl, M.; Mihokova, E.; Nitsch, K.; Somma, F.; Giampaolo, C.; Pazzi, G. P.; Fabeni, P.; Zazubovich, S. Photoluminescence of $Cs_4PbBr_6$ Crystals and Thin Films. *Chem. Phys. Lett.* **1999**, *306*, 5−6.
(31) Lin, H.; Zhou, C.; Tian, Y.; Siegrist, T.; Ma, B. Low-Dimensional Organometal Halide Perovskites. *ACS Energy Lett.* **2018**, *3* (1), 54−62.
(32) Saidaminov, M. I.; Mohammed, A. F.; Bakr, A. M. Low-Dimensional-Networked Metal Halide Perovskites: The Next Big Thing. *ACS Energy Lett.* **2017**, *2* (4), 889−896.
(33) Bohun, A.; Dolejsi, J.; Barta, C. The Absorption and Luminescence of $(PbCl_6)^{4-}$ and $(PbBr_6)^{4-}$ Complexes. *Czech. J. Phys. B* **1970**, *20*, 803−807.
(34) Jacobs, P. W. M. Alkali Halide Crystals Containing Impurity Ions with the $Ns^2$ Ground-State Electronic Configuration. *J. Phys. Chem. Solids* **1991**, *52* (1), 35−67.
(35) Ranfagni, A.; Mugnai, D.; Bacci, M.; et al. The Optical Properties of Thallium-Like Impurities in ALkali-Halide Crystals. *Adv. Phys.* **1983**, *32* (6), 823−905.
(36) Forro, M. Uber die Absorptionspektra Einiger Alkalihalogenidphosphore Bei Hohen Temperaturen. *Z. Phys.* **1929**, *56*, 534−543.
(37) Blasse, G. Optical Electron Transfer between Metal Ions and Its Consequences Springer: Berlin, Heidelberg pp 153−187.
(38) Folkerts, H. F.; Hamstra, M. A.; Blasse, G. The Luminscence of $Pb^{2+}$ in Alkaline Earth Sulfates. *Chem. Phys. Lett.* **1995**, *246*, 135−138.
(39) Zhang, Y.; Saidaminov, M. I.; Dursun, I.; Yang, H.; Murali, B.; Alarousu, E.; Yengel, E.; Alshankiti, B. A.; Bakr, A. M.; Mohammed, A. F. Zero-Dimensional $Cs_4PbBr_6$ Perovskite Nanocrystals. *J. Phys. Chem. Lett.* **2017**, *8* (5), 961−965.
(40) Liu, Z.; Bekenstein, Y.; Ye, X.; Nguyen, S. N.; Swabeck, J.; Zhang, D.; Lee, S. T.; Yang, P.; Ma, W.; Alivisatos, A. P. Ligand Mediated Transformation of Cesium Lead Bromide Perovskite Nanocrystals to Lead Depleted $Cs_4PbBr_6$ Nanocrystals. *J. Am. Chem. Soc.* **2017**, *139* (15), 5309−5312.
(41) Yin, J.; Zhang, Y.; Bruno, A.; Soci, C.; Bakr, A. M.; Bredas, J. L.; Mohammad, A. F. Intrinsic Lead ion Emission in Zero-Dimensional $Cs_4PbBr_6$ Nanocrystals. *ACS Energy Lett.* **2017**, *2* (12), 2805−2811.
(42) Wang, X.; Liu, Y.; Liu, N.; Sun, R.; Zheng, W.; Liu, H.; Zhang, Y. Revisiting the nanocrystal formation process of zero-dimensional perovskite. *J. Mater. Chem. A* **2021**, *9*, 4658−4663.
(43) Cai, H.; Lao, M.; Xu, J.; Chen, Y.; Zhong, C.; Lu, S.; Hao, A.; Chen, R. All-Inorganic Perovskite $Cs_4PbBr_6$ Thin Films in Optoelectronic Resisitve Switching Memory Devices with a Logical Application. *Ceram. Int.* **2019**, *45* (5), 5724−5730.
(44) Cha, J. H.; Han, J. H.; Yin, W.; Park, C.; Park, Y.; Ahn, T. K.; Cho, J. H.; Jung, D. Y. Photoresponse of $CsPbBr_3$ and $Cs_4PbBr_6$ Perovskite Single Crystals. *J. Phys. Chem. Lett.* **2017**, *8* (3), 565−570.
(45) Chen, X.; Zhang, F.; Ge, Y.; Shi, L.; Huang, S.; Tang, J.; Lv, Z.; Zhang, L.; Zou, B.; Zhong, H. Centimeter-Sized $Cs_4PbBr_6$ Crystals with Embedded $CsPbBr_3$ Nanocrystals Showing Superior Photoluminescence: Nonstoichiometry Induced Transformation and Light-Emitting Applications. *Adv. Funct. Mater.* **2018**, *28*, 1706567.
(46) Saidaminov, M. I.; Almutlaq, J.; Sarmah, S.; Dursun, I.; Zhumekenov, A. A.; Begum, R.; Pan, J.; Cho, N.; Mohammed, A. F.; Bakr, A. M. Pure $Cs_4PbBr_6$: Highly Luminescent Zero-Dimensional Perovskite Solids. *ACS Energy Lett.* **2016**, *1* (4), 840−845.
(47) Zhou, Y.; Ding, J.; Wang, Z.; Tong, Y.; Liang, X.; Du, J.; Xia, W.; Liu, Z.; Xiang, W. Ultrastable EVA Film-Protected $Cs_4PbBr_6$ Solid Powder for Wide Color Gamut Blacklight Display and Upconversion Emission. *Chem. Eng. J.* **2021**, *426*, No. 130786.
(48) Bao, Z.; Wang, H.-C.; Jiang, Z.-F.; Chung, R. J.; Liu, R.-S. Continuous Synthesis of Highly Stable $Cs_4PbBr_6$ Perovskite Microcrystals by a Microfluidic System and Their Application in Whit-Light-Emitting Diodes. *Inorg. Chem.* **2018**, *57* (21), 13071−13074.
(49) Chen, Y.-M.; Zhou, Y.; Zhao, Q.; Zhang, J.-Y.; Ma, J.-P.; Xuan, T.-T.; Guo, S.-Q.; Yong, Z.-J.; Wang, J.; Kuroiwa, Y.; et al. $Cs_4PbBr_6$/$CsPbBr_3$ Perovskite Composites with Near-Unity Luminescence Quantum Yield: Large-Scale Synthesis, Luminescence and Formation Mechanism, and White Light Emitting Diode Application. *ACS Appl. Mater. Interfaces* **2018**, *10* (18), 15905−15912.
(50) Zhao, H.; Sun, R.; Wang, Z.; Fu, K.; U, X.; Zhang, Y. Zero-Dimensional Perovskite Nanocrystals for Efficient Luminescent Solar Concentrators. *Adv. Funct. Mater.* **2019**, *29* (30), No. 1902262.
(51) Liu, Y.; Li, N.; Sun, R.; Zheng, W.; Liu, T.; Li, H.; Chen, Y.; Liu, G.; Zhao, H.; Liu, H. Stable metal-halide perovskites for luminescent solar concentrators of real-device integration. *Nano Energy* **2021**, *85*, No. 105960.
(52) Akkerman, Q. A.; Abdelhady, A. L.; Manna, L. Zero-Dimensinoal Cesium Lead Halides: History, Properties, and Challenges. *J. Phys. Chem. Lett.* **2018**, *9* (9), 2326−2337.
(53) Cha, J. H.; Lee, H. J.; Kim, S. H.; Ko, K. C.; Suh, B. J.; Han, O. H.; Jung, D. Y. Superparamagnetism of Green Emissive $Cs_4PbBr_6$ Zero-Dimensional Perovskite Crystals. *ACS Energy Lett.* **2020**, *5* (7), 2208−2216.
(54) Wang, K.; Yuan, Y.; Du, S.; Yao, Q.; Zhang, J.; Chang, J.; Shang, C.; Li, C.; Sun, H.; Zhang, W.; Ding, J. Understanding of the Photoluminescence Mechanism Based on Zero-DImensional $Cs_4PbBr_{6-m}X_m$ (X = Cl, I) Single Crystals. *J. Phys. Chem. C* **2021**, *125* (28), 15223−15232.
(55) Seth, S.; Samanta, A. Fluorescent Phase-Pure Zero-Dimensional Perovskite Related $Cs_4PbBr_6$ Microdisks: Synthesis and Single-Particle Imaging Study. *J. Phys. Chem. Lett.* **2017**, *8* (18), 4461−4467.
(56) Qin, Z.; Dai, S.; Hadjiev, V. G.; Wang, C.; Xie, L.; Ni, Y.; Wu, C.; Yang, G.; Chen, S.; Deng, L.; et al. Revealing the Origin of Luminescence Center in 0D Cs4PbBr6 Perovskite. *Chem. Mater.* **2019**, *31* (21), 9098−9104.
(57) Zhang, Z.; Zhu, Y.; Wang, W.; Zheng, W.; Lin, R.; Li, X.; Zhang, H.; Zhong, D.; Huang, F. Aqueous Solution Growth of Millimeter-Sized nongreen-Luminescent Wide Bandgap $Cs_4PbBr_6$ Bulk Crystal. *Cryst. Growth Des.* **2018**, *18* (11), 6393−6398.

(58) Quan, L. N.; Quintero-Bermudez, R.; Voznyyy, O.; Walters, G.; Jain, A.; Fan, J. Z.; Zheng, X.; Yang, Z.; Sargent, E. H. Highly Emissive Green Perovskite Nanocrystals in a Solid State Crystalline Matrix. *Adv. Mater.* **2017**, *29* (21), No. 1605945.
(59) Ray, A.; Maggioni, D.; Baranov, D.; Dang, Z.; Prato, M.; Akkerman, Q. A.; Goldoni, L.; Caneva, E.; Manna, L.; Abdelhady, A. L. Green-Emitting Powders of Zero-Dimensional $Cs_4PbBr_6$: Delineating the Intricacies of the Synthesis and the Origin of Photoluminescence. *Chem. Mater.* **2019**, *31* (18), 7761−7769.
(60) Riesen, N.; Lockrey, M.; Badek, K.; Riesen, H. On the Origins of the Green Luminscence in the ""Zero-Dimensional Perovskite"$Cs_4PbBr_6$": Conclusive Results from Cathodoluminescence Imaging. *Nanoscale* **2019**, *11*, 3925.
(61) Wang, L.; Liu, H.; Zhang, Y.; Mohammed, A. F. Photoluminescence Origin of Zero-DImensional $Cs_4PbBr_6$ Perovskite. *ACS Energy Lett.* **2020**, *5* (1), 87−99.
(62) Biswas, K. Revisiting the Origin of Green Emission in $Cs_4PbBr_6$. *Mater. Adv.* **2022**, *3* (17), 6791−6798.
(63) Cola, M.; Massarotti, V.; Riccardi, R.; Sinistri, C. Binary Systems Formed by Lead Bromide with (Li, Na, K, Rb, Cs, and Tl)Br: a DRA and Diffractometric Study. *Z. Naturforsch., A* **1971**, *26.8*, 1328−1332.
(64) Nikl, M.; Nitsch, K.; Mikokova, E.; Polak, K.; Fabeni, P.; Pazzi, G. P.; Gurioli, M.; Santucci, S.; Phani, R.; Scacco, A.; et al. Lumienscence of $CsPbBr_3$-Like Quantum Dots in CsBr Single Crystals. *Phys. E: Low-Dimens. Syst. Nanostruct.* **1999**, *4* (4), 323−331.
(65) Aceves, R.; Babin, V.; Barboza Flores, M.; Fabeni, P.; Maaroos, A.; Nikl, M.; Nitsch, K.; Pazzi, G. P.; Perez Salas, R.; Sildos, I.; et al. Spectroscopy of $CsPbBr_3$ Quantum Dots in CsBr:Pb Crystals. *J. Lumin.* **2001**, *93* (1), 27−41.
(66) Nikl, M.; Nitsch, K.; Polak, K.; Mihokova, E.; Zazubovich, S.; Pazzi, G. P.; Fabeni, P.; Salvini, L.; Aceves, R.; Barbose-Flores, M.; et al. Quantum Size Effect in the Excitonic Luminescence of $CsPbX_3$-Like Quantum Dots in CsX (X = Cl, Br) Single Crystal Host. *J. Lumin.* **1997**, *72*−*74*, 377−379.
(67) van Hattem, A.; Alders, D.; konings, R. J. M.; Smith, A. L. Ternary System CsI-$PbI_2$-$BiI_3$ and Thermodynamic Stability of Cesium Metal Halide Perovskites. *J. Phys. Chem. C* **2023**, *127* (35), 17482−17496.
(68) Kang, B.; Biswas, K. Exploring Polaronic, Excitonic Structures and Luminescence in $Cs_4PbBr_6$/$CsPbBr_3$. *J. Phys. Chem. Lett.* **2018**, *9* (4), 830−836.
(69) Rietveld, H. M. A Profile Refinement Method for Nuclear and Magnetic Structures. *Appl. Crystallogr.* **1969**, *2*, 64−71.
(70) van Laar, B.; Schenk, H. The Development of Powder Profile Refinement at the Reactor Centre Nehterlands at Petten. *Acta Crystallogr., Sect. A: Found. Adv.* **2018**, *74.2*, 88−92.
(71) Rodríguez-Carvajal, J. LLB Sacley and LCSIM Rennes. 2003.
(72) Roisnel, T.; Rodríguez-Carvajal, J.A Windows Tool for Powder Diffraction Patterns Analysis, Material Science Forum. In *Proceedings of the European Powder Diffraction Conference (EPDIC7)* 2000; pp 118−123.
(73) Kubota, T.; Yanagimoto, S.; Saito, H.; Akiba, K.; Ishii, A.; Sannomiya, T. Chatodoluminscence Spectral and Lifetime Mapping of $Cs_4PbBr_6$: Fast Lifetime and its Scintillator Application. *Appl. Phys. Express* **2024**, *17*, No. 015005.
(74) Ding, Y.; Lin, R.; Lioang, Y.; Zheng, W.; Chen, L.; Ouyang, X.; Huang, F. High-Efficiency Down-Conversion Radiation Fluorescence and Ultrafast Photoluminscence (1.2 ns) at the Interface of Hybrid $Cs_4PbBr_6$ - CsI Nanocrystals. *J. Phys. Chem. Lett.* **2021**, *12* (30), 7342−7349.
(75) Li, Y.; Chen, L.; Liu, B.; Ruan, J.; Liu, J.; Ouyang, X.; Xu, Q. The Phosphorescence Emission in Undoped Lead-Halide $Cs_4PbvBr_6$ Single Crystals at Low Temperature. *Ceram. Int.* **2022**, *48* (12), 16730−16736.
(76) Wu, X.; Zhou, Q.; Wu, H.; Du, X.; Niu, G.; Liang, G.; Hy, Q.; Xiao, J. $Cs_4PbBr_{6-x}Cl_x$ Single Crystals with Tunable Emission for X-ray Detection and Imaging. *J. Phys. Chem. C* **2021**, *125*, 26619−26626.
(77) Collins, P. R.; Fredericks, W. J. Absorption Spectra and Oscillator Strength of KBr:Pb. *J. Phys. Chem. Solids* **1986**, *47* (5), 529−532.
(78) Sastry, S. B. S.; Viswanathan, V.; Ramasastry, C. Lead Centres in Alkali Halides: NaCl, KCl and KBr. *J. Phys. Soc. Jpn.* **1973**, *35*, 508−513.
(79) Nikl, M.; Mihokova, E.; Nitsch, K. Photoluminescence and Decay Kinetics of $Cs_4PbCl_6$ Single Crystals. *Solid State Commun.* **1992**, *4* (12), 1089−1092.
(80) Zazubovich, S. Polarization Spectroscopy of $ns^2$ Impurity Ions in Alkali Halides. *Int. J. Modern Phys. B* **1994**, *08* (8), 985−1031.
(81) Bol, A. A.; Meijerink, A. Luminescence of Nanocrystaline ZnS:$Pb^{2+}$. *Phys. Chem. Chem. Phys.* **2001**, *3*, 2105−2112.
(82) Goovaerts, E.; Nistor, S. V.; Schoemaker, D. Electron-Spin Resonance of a Complex $Pb^+$ ($6p^1$) Defectr in Alkali Halides. *Phys. Rev. B* **1983**, *28*, 3712.
(83) Kerssen, J.; De Gruijter, W. G.; Volger, J. EPR of $Pb^+$ Ions and Exchange-Coupled $Pb^+$ Ion Pairs in U.V.-Irradiated $PbCl_2$ and $PbBr_2$ Crystals. *Physica* **1973**, *70* (2), 375−396.
(84) Fabeni, P.; Krasnikov, A.; Nikl, M.; Pazzi, G. P.; Zazubovich, S. Stimulated Self-Trapped Exciton Emission in CsI:Pb. *Solid State Commun.* **2003**, *126* (12), 665−669.
(85) Egemberdiev, Zh.; Nagirnyi, V.; Soovik, T.; Zazubovich, S. Decay Kinetics and Polarization of the $A_T$ Emission of $Pb^{2+}$ Centres of Different STructure in KBr:$PbBr_2$. *Phys Status Solid (b)* **1984**, *126* (1), 407−414.
(86) Egemberdiev, Zh.; Usarov, S.; Zazubovich, S. Luminescene of Lead Ions Associated with Interstitials and Vacancies in Alkali Halides. *Phys Status Solid (b)* **1991**, *164* (1), 195−206.
(87) Egemberdiev, Zh.; Ismailov, K.; Usarov, A.; Zazubovich, S.; Jaanson, N. Luminescent Associates of $Pb^{2+}$ $V_c^-$ Dipoles with Interstitial Iodine Atoms in KI:$PbI_2$ Crystals. *Phys Status Solid (b)* **1991**, *163* (1), 183−190.
(88) Nagli, L. E.; Dyachenko, S. V. Influence of a $V_c^-$ Vacancy on Luminescence of $Pb^+$ Centres in Alkali Halides. *Basic Solid State Phys.* **1988**, *146* (1), 295−301.
(89) van Dijken, A.; Folkerts, H. F.; Blasse, G. Evidence for D-band Emission from $Pb^{2+}$ in Alkaline-Earth Fluorohalides with the PbFCl Struvture. *J. Lumin.* **1997**, *72*−*74*, 660−661.
(90) Folkerts, H. F.; Ghianni, F.; Blasse, G. Search for D-level Emission of $Pb^{2+}$ in Alkaline-Earth Aluminates and Gallates. *J. Phys. Chem. Solids* **1996**, *57* (11), 1659−1665.
(91) Folkerts, H. F.; van Dijken, A.; Blasse, G. Two Types of Luminescence from $Pb^{2+}$ in Alkaline-Earth Fluorohalides with the PbFCl Structure. *J. Phys.: Condens. Matter* **1995**, *7* (50), No. 10049.
(92) Almeida, G.; Goldoni, L.; Akkerman, Q.; Dang, Z.; Khan, A. H.; Marras, S.; Moreels, I.; Manna, L. Role of Acid-Base Eqwuilibira in the Size, Shape, and Phase Contril of Cesium Lead Bromide Nanocrystals. *ACS Nano* **2018**, *12* (2), 1704−1711.
(93) He, Y.; Matei, L.; Jung, H. J.; McCall, K. M.; Chen, M.; Stoumpos, C. C.; Liu, Z.; Peters, J. A.; Chung, D. Y.; Wessels, B. W.; et al. High Spectral Resolution of Gamma-Rays at Room Temperature by Perovskite $CsPbBr_3$ Single Crystals. *Nat. Commun.* **2018**, *9*, No. 1609.
(94) shin, M.; Nam, S. W.; Sadhanala, A.; Shivanna, R.; Anaya, M.; Jimenez-Solano, A.; Yoon, H.; Jeon, S.; Stranks, S. D.; Hoye, R. L. Z.; et al. Understanding the Origin of ultrasharp Sub-Bandgap Luminscence from Zero-Dimensional Inorganic Perovskite $Cs_4PbBr_6$. *ACS Appl. Energy Mater.* **2020**, *3* (1), 192−199.
(95) Williams, R. T.; Grim, J. Q.; Li, Q.; Ucer, K. B.; Moses, W. W. Excitation Density, Diffusion-Drift, and Proportionality in Scintillators. *Phys Status Solid (b)* **2011**, *248*, 426−438.
(96) Moses, W. W.; Bizarri, G.; Williams, R. T.; Payne, S. A.; Vasilev, A. N.; Singh, J.; Li, Q.; Grim, J. Q.; Choong, W.-S. The Origins of Scintillator Non-Proportionality. *IEEE Trans. Nucl. Sci.* **2012**, *59*, 2038−2044.
(97) Vasil'ev, A. N. From Luminscence Non-Linearity to Scintillation Non-Proportionality. *IEEE Trans. Nucl. Sci.* **2008**, *55* (3), 1054−1061.


https://doi.org/10.1021/acs.jpcc.4c06347
J. Phys. Chem. C 2024, 128, 19921−19932

(98) Khodyuk, I. V. Nonproportionality of inorganic scintillators DOI: 10.4233/uuid:cb4008a8-981a-4283-b213-199d41756269.



https://doi.org/10.1021/acs.jpcc.4c06347
J. Phys. Chem. C 2024, 128, 19921−19932